

COMPUTATIONAL MODELING OF THE CLASS I LOW-MASS PROTOSTAR ELIAS 29 APPLYING OPTICAL CONSTANTS OF ICES PROCESSED BY HIGH ENERGY COSMIC RAY ANALOGS

W. R. M. ROCHA AND S. PILLING

Instituto de Pesquisa & Desenvolvimento, Universidade do Vale do Paraíba, São José dos Campos,
 SP 12244000, Brazil; willrobson88@hotmail.com, sergiopilling@yahoo.com.br
 Received 2014 June 9; accepted 2015 January 27; published 2015 April 8

ABSTRACT

We present a study of the effects of high energy cosmic rays (CRs) over the astrophysical ices, observed toward the embedded class I protostar Elias 29, by using computational modeling and laboratory data. Its spectrum was observed with the *Infrared Space Observatory* (ISO) covering 2.3–190 μm . The modeling employed the three-dimensional Monte Carlo radiative transfer code RADMC-3D and laboratory data of bombarded ice grains by CR analogs and unprocessed ices (not bombarded). We are assuming that Elias 29 has a self-irradiated disk with inclination $i = 60^\circ$, surrounded by an envelope with a bipolar cavity. The results show that absorption features toward Elias 29 are better reproduced by assuming a combination between unprocessed astrophysical ices at low temperature (H_2O , CO, CO_2) and bombarded ices ($\text{H}_2\text{O}:\text{CO}_2$) by high energy CRs. Evidences of the ice processing around Elias 29 can be observed by the good fitting around 5.5–8.0 μm , by polar and apolar ice segregation in 15.15–15.25 μm , and by the presence of the CH_4 and HCOOH ices. Given that non-nitrogen compounds were employed in this work, we assume that absorption around 5.5–8.0 μm should not be associated with the NH_4^+ ion (see the 2003 work of Shutte & Khanna), but more probably with aliphatic ethers (e.g., R1-OCH₂-R2), CH_3CHO , and related species. The results obtained in this paper are important because they show that the environment around protostars is better modeled considering processed samples and, consequently, demonstrate the chemical evolution of the astrophysical ices.

Key words: protoplanetary disks – ISM: molecules – radiative transfer – methods: laboratory: molecular – stars: individual (Elias 29)

1. INTRODUCTION

The star formation process takes place inside molecular clouds, where dense cores collapse to form young stellar objects (YSOs), which are often called protostars. Following the initial contraction phase these objects continue their physical evolution. Several observations and computational models have shown that protostars can be classified in four classes, Class 0–III (Lada & Wilking 1984; Lada 1987), which suggests an evolutionary sequence among them. A Class I source, which is the subject of this paper, is a T Tauri star surrounded by an infalling envelope, which in some cases has bipolar cavities. Scatter light models show that cavities are necessary to better fit the observed flux in the near-infrared (near-IR; Kenyon et al. 1993; Whitney et al. 1997). In addition to the physical evolution of young stars, their environment evolves chemically, due to the rich physicochemical processes that exist among gases, ices, and high energy radiation.

In the densest regions of the protostellar disk and envelope, the molecules in the gas phase can condense onto dust grains by an adsorption process, such as physisorption and chemisorption, forming ice mantles. Once formed, the astrophysical ices (as they are also called) can be subjected to FUV or X-ray radiation due to the protostar, as well as bombardment by cosmic rays (CRs) from the interstellar medium. Such interactions are important because they can change ice mantle properties, as well as return molecules (and new molecules) to the gas phase by desorption processes (Tielens & Charnley 1997; van Dishoeck & Blake 1998). In other words, the ices experienced chemical changes by thermal or radiative processing. However, having average energies of several MeV, the CRs are able to penetrate deeply into the envelope or disk, compared to FUV or X-rays photons. Therefore, since the ices

are formed in the densest parts of the disk or envelope, the chemical effects driven by FUV or X-rays photons on the ices are very small compared with CRs. Instead, such photons are very important to regulate the gas-phase chemistry, as for example, to dissociate molecules (HCN , H_2O , CO, H_2) or ionize He, considering X-rays (Henning & Semenov 2013).

Pilling et al. (2010a, 2010b, 2012) suggested that the bombardment of ices by CR analogs may help to justify some features in the infrared spectra of YSOs. In addition, as discussed by Pilling et al. (2011), the chemistry of the ice depends on the temperature in addition to the stellar radiation field (IRF) or interstellar radiation field. A recent paper from Cleaves et al. (2014) highlights the importance of CRs for the enhancement of the chemistry inside protoplanetary disks. The authors shows that, if a model does not contain CRs as an ionizing factor, then the ionization level in the internal regions of the disk is too small to support a high rate of ion-molecule reactions.

The protostar Elias 29 (Elias 1978), also known as Elias 2–29 and WL 15 (Wilking & Lada 1983), is located in the ρ Ophiuchi molecular cloud and is classified as a class I YSO with an age range of $0.4\text{--}5 \times 10^5$ yr (Chen et al. 1995; Boogert et al. 2000; Enoch et al. 2009). The coordinates of Elias 29 (J2000) are $\alpha = 16^{\text{h}}27^{\text{m}}09^{\text{s}}.3$ and $\delta = -24^\circ37'21''$. Despite several investigations, the distance and luminosity of this object given in the literature are still quite divergent: $d \sim 160$ pc (Whittet 1974; Boogert et al. 2000, 2002a), $d \sim 125 \pm 25$ pc (de Geus et al. 1989; Lommen et al. 2008), $L = 36 L_\odot$ (Chen et al. 1995; Boogert et al. 2000, 2002a), and $L = 13.6 L_\odot$ (Evans et al. 2003; Lommen et al. 2008). Elias 29 is also surrounded by several other YSOs presents in the ρ Ophiuchi molecular cloud.

The inclination of Elias 29 has been estimated from spectroscopic features and more recently from images obtained by Huélamo et al. (2006). Kenyon et al. (1993) argue that deep absorption silicate bands, such as those observed in Elias 29, are typical of a disk with edge-on inclination. However, studies from Boogert et al. (2002a) show that due to flatness of the Elias 29 spectrum, from 4 to 100 μm , the disk inclination must be less than 60° . From this result, the deep absorption features observed from spectral energy distribution (SED) due to ices and silicate, must originate in the envelope or foreground clouds found in the same study. In this work, we adopt a fiducial inclination of $i = 60^\circ$, as for example, Lommen et al. (2008) and Miotello et al. (2014). In the studies from Huélamo et al. (2006), the authors obtained a direct image of Elias 29 using a polarimetric differential technique with a NAOS–CONICA (NACO) instrument and adaptive optics facility from the Very Large Telescope. Their results show that a full edge-on inclination is improbable for Elias 29. Besides the presence of the disk, the authors also detected in the near-IR (H and K bands) a bipolar hydrogen molecular outflow in the NW–SE direction (assuming N to the top and E to the left) and a dark lane in the NE–SW direction. The presence of CO and molecular hydrogen was also observed in the outflows of Elias 29 by Gómez et al. (2003), and Zhang et al. (2013), respectively.

Öberg et al. (2011) and references therein show that most abundant molecular species around low and high mass young stars are H_2O , CO, CO_2 , CH_3OH , NH_3 , CH_4 , and OCN^- . By using spectral data from the *Infrared Space Telescope* (ISO), Boogert et al. (2000) has shown that the inventory of ices around Elias 29 is composed mainly of H_2O , CO, and CO_2 . However, several absorption features between 5.5 and 8.0 μm were also observed toward this source, including the prominent band at 6.85 μm . This last feature has often been attributed to the NH_4^+ ion (Demyk et al. 1998; Hudson et al. 2001; Shutte & Khanna 2003). However in many cases the condensation of gas over dust grains leads to the formation of dirty ices, such as $\text{H}_2\text{O}:\text{CO}_2$ (Öberg et al. 2011). Once the different molecular species are trapped in the same ice matrix, the chemistry induced by high energy radiation should be rich. Nevertheless, it is not conclusive from Boogert et al. (2002a) whether the ices in the disk or envelope have experienced some interaction with high energy radiation, inducing chemical changes in their properties.

In this paper, we investigate whether the ices observed toward Elias 29 show evidence of thermal or radiative processing due to an interaction with high energy CRs coming from the interstellar medium. We present a better model for Elias 29 SED and the resolved simulated IR images (from near- to far-IR). The general parameters that constrain our modeling were obtained from observational data in the IR taken from the literature (Boogert et al. 2002a; Huélamo et al. 2006; Beckford et al. 2008; Lommen et al. 2008; Miotello et al. 2014). The model was built by employing the radiative transfer code RADMC-3D¹ (C. P. Dullemond, in preparation), assuming the presence of not bombarded ices (unprocessed ices; Rocha & Pilling 2014) and bombarded ices by CR analogs (processed ices; Pilling et al. 2010a) distributed by the protostellar disk and envelope. By using the temperature of the disk and envelope calculated by the RADMC-3D code, the position of

the ices employed in the modeling were fixed because the ices cannot occupy regions where the temperature is enough to return the frozen molecules to the gas phase. For comparison, we also show the fit for the model using only unprocessed ices, which is an usual method observed in the literature (e.g., Boogert et al. 2002a; Pontoppidan et al. 2005). However, this methodology cannot reproduce the chemical evolution features observed in the Elias 29 spectrum. This paper shows that a powerful radiative transfer code combined with processed ices to simulate the chemical evolution of the astrophysical ices is fundamental to better characterize the protostellar environment. Such evidence of the chemical evolution of the ices around Elias 29 is given by the presence of several absorption features between 5.5–8.0 μm , such as CH_4 and HCOOH , and by the polar and apolar ice segregation, seen by the splitted profile at 15.15 and 15.25 μm . Furthermore, we show that absorption bands between 5.5 and 8.0 μm are better related with CH bonds than the NH_4^+ ion. Additionally, in this work we verified which dust grain size better fits the observed spectrum of Elias 29 in the infrared.

This paper is structured as follows. In Section 2 we present how the observation and laboratory data were obtained and how the modeling was employed. Section 3 shows the results of this paper.

2. METHODOLOGY

2.1. Observations

2.1.1. Elias 29 SED

The spectrum used in this paper for Elias 29 was obtained from the public database of the *Infrared Space Observatory* (ISO) observed with two instruments:² the Short Wavelength Spectrometer (SWS; de Graauw et al. 1996) for 2.3–45 μm and the Long Wavelength Spectrometer (LWS; Clegg et al. 1996) for 45–190 μm . The power resolutions $R = \lambda/\Delta\lambda$ are $R_{\text{SWS}} = 400$ and $R_{\text{LWS}} = 200$, respectively. The *exposure times* using each instrument on the target were 3454 and 2611 s, respectively.

The spectrum was reduced automatically using the offline-processing package. As informed in the online database, the two spectra have good quality, without dark current problems, and are scientifically validated. Additional information about the reduction processing can be found in ISO Data Analysis Software³ and Boogert et al. (2000). Figure 1(a) presents a field of view (FOV) of 38×32 arcmin taken from MIPS camera in 24 μm from the *Spitzer Space Telescope*. This image shows a very dense region with several embedded sources, where Elias 29 is indicated by a red arrow. Figure 1(b) shows the IR spectrum of Elias 29 obtained from ISO (SWS + LWS), which is dominated by absorption bands due to silicate and ices along the line of sight. In addition to strong bands observed in this spectrum, other weak features are also detected (Boogert et al. 2000).

2.1.2. IRAC Bands Photometry

To determine the evolutionary stage of Elias 29, images of the ρ Ophiuchi cloud were taken from a public archive of the IRAC/*Spitzer* camera in four filters (3.6, 4.5, 5.8, and 8.0 μm).⁴

¹ <http://www.ita.uni-heidelberg.de/~dullemond/software/radmc-3d/>

² <http://iso.esac.esa.int/>

³ <http://iso.esac.esa.int/archive/software/>

⁴ <http://sha.ipac.caltech.edu>

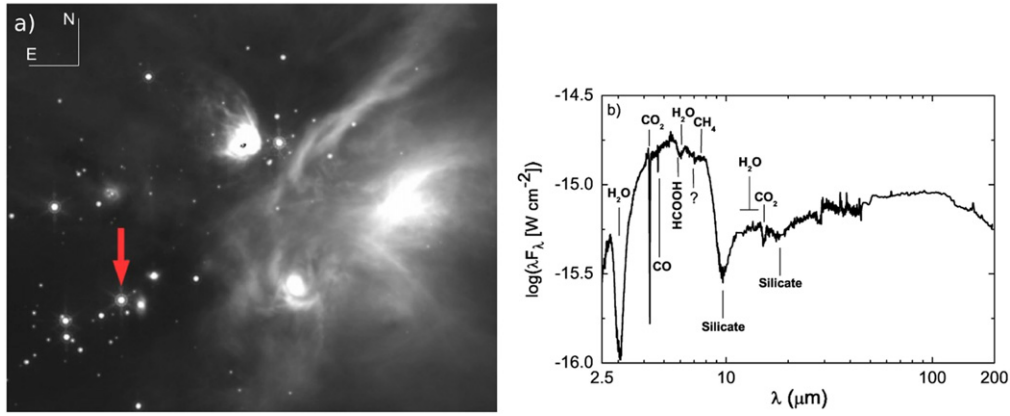


Figure 1. (a) Rho ophiuchi molecular cloud region containing the low mass protostar Elias 29 (red arrow). (b) IR spectrum of Elias 29 obtained from *ISO* observations (SWS + LWS). The strong absorption features due to silicate and ices are indicated. The question mark indicates the small absorption band in $6.85 \mu\text{m}$ (1459.8 cm^{-1}), which remains without conclusive assignment.

Photometric and instrumental corrections have previously been made (Fazio et al. 2003; Hora et al. 2008).

The astrometry and photometry of each image were performed using the Starfinder code (Diolaiti et al. 2000) by PSF fitting. This procedure allowed us to build a color-color diagram and determine the evolutionary stage of Elias 29, as shown in Figure 2.

The boundary boxes were taken from Megeath et al. (2004) to define the regions for YSO class I and II. This diagram also shows that the Elias 29 classification agrees with a previous study using a Bolometric Luminosity and Temperature diagram from Chen et al. (1995); therefore, it can definitively be classified as a class I protostar.

2.2. Opacity Calculation

One of the most important parameters of radiative transfer models is the optical constants (refractive index) of the matter. However, physical properties such as the size and geometry of absorbers (grains) and their temperature are also essential. Such parameters can be considered as one simple parameter: opacity. Because opacity parameters are a key part of the radiative transfer calculation, we show how they were calculated, considering two models for the nature of the grain around Elias 29. In this work, the label “Model 1” refers to opacities of only unprocessed ices and “Model 2” refers to more realistic ices that were previously processed by CR analogs (taken from Pilling et al. 2010a), combined with unprocessed ices.

In Model 1, we adopted the usual methodology from the literature (Pontoppidan et al. 2005), using only unprocessed ices composed of H_2O , CO_2 , CO , and silicate (MgFeSiO_4), combined with amorphous carbon. The more realistic approach, described by Model 2, supposes that a fraction of the material was processed by energetic CRs coming from the interstellar medium. In this case, Model 2 takes into account a processed mixture of $\text{H}_2\text{O}:\text{CO}_2$ (1:1; Pilling et al. 2010a) in addition to pure grains of H_2O , CO_2 , CO , and silicate. Previous papers usually use the opacities of coagulated grains from Ossenkopf & Henning (1994) and Weingartner & Draine (2001) to simulate the presence of the grains and ices in the interstellar medium. In this paper, such data cannot be applied because we are using processed ices, which are not available in the literature.

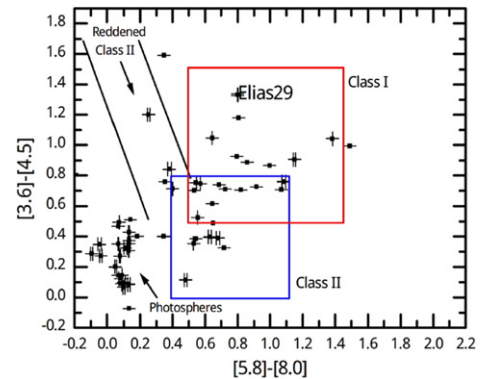


Figure 2. Color-color diagram for the ρ Ophiuchi cloud. The boxes define regions for YSO class I and II. The black lines identify reddened class II protostars. The photospheres are main sequence stars or YSO class III. Elias 29 is classified as a Class I protostar and is indicated by its name.

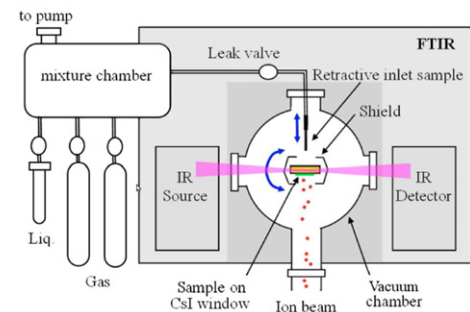


Figure 3. Schematic diagram of the experimental setup. The ice is deposited on the substrate (e.g., ZnSe) where it is condensed due to lower temperature (generally $\sim 10 \text{ K}$). The infrared spectroscopy is used to detect the absorption bands before and after the irradiation of the ice with the ion beam. Extracted from Pilling et al. (2010a).

2.2.1. Laboratory Experiments

In the interstellar medium, frozen molecules on the dust grains are exposed to ionizing radiation, which triggers physicochemical processes allowing chemical changes. Such processes can be reproduced in the laboratory, leading to the understanding of how the chemistry in the star-forming regions and their environment evolves.

A typical setup of the experiment is presented in Figure 3. Briefly, the samples were deposited onto substrates (e.g., CsI ,

ZnSe) previously cooled to cryogenic temperatures (~ 10 K), in the high vacuum regime ($p < 10^8$ mbar). Using this procedure, the molecules from gas or liquid are condensed to represent the astrophysical ices. During the experiments, these ices can be bombarded by the CR analogs or photons to simulate different input energies coming from the interstellar medium or young star. Fourier Transform InfraRed spectroscopy (FTIR) was used as a diagnostic tool to detect the molecular absorption bands in the sample.

In this paper, the astrophysical ices used in Models 1 and 2 were simulated in the laboratory to obtain the absorbance data in the infrared. The experimental procedure employed for non-bombarded ices can be found in Rocha & Pilling (2014), and in Pilling et al. (2010a) for the processed ice. The processed ices employed in this work (Model 2) were obtained from the mixture of H_2O and CO_2 , bombarded with heavy ions ($^{58}\text{Ni}^{13+}$ ion projectiles with energies of 52 MeV) up to a final fluence equal to 1×10^{13} ions cm^{-2} (Pilling et al. 2010a), to simulate the effects of the high energy CRs. At the end of the experiment the formation of new infrared bands associated with new molecular species was observed.

Details about the chemistry behind the ice processing by CRs can be found in Bennett et al. (2005) and Pilling et al. (2010a, 2010b, 2011). In summary, if CR particles penetrate into ice-forming regions they lose their energy almost exclusively due to the electronic interaction with the target molecules, which allows a temperature increase, among other effects. Such energy exchange may be enough to break the chemical bonds of the molecules in the solid phase and allow for the formation of new molecular species.

2.2.2. Dust Model

Because it is necessary to model the ices and silicate abundances independently for Elias 29, the opacities were calculated for each species using the results from experiments in the laboratory and the optical constants as input data. The first step was to calculate the optical constants of the ices, given by equation $\mathbf{m} = n + ik$, where the n value represents the real part and k values the complex part; both are a function of the wavelength. They were calculated directly from absorbance data in the infrared obtained from experimental works. This procedure was performed with the NKABS code, which is a free code developed in Python Programming Language (Rocha & Pilling 2014). This code is based on the Lambert–Beer law, Kramers–Kronig relationship, and McLaurin’s methodology. Figure 4 presents the graphics for the optical constants of grain employed in this paper. The values for CO ice and silicate and amorphous carbon dust were taken from an online database.^{5,6,7}

After the calculation of optical constants (refractive index in the infrared), the absorption and scattering opacities of the dust and ices were calculated employing the Mie theory. To proceed with the calculations, we assumed that the grains are spherical, with sizes defined by a MRN distribution and given by a power law, $dN(a)/da \propto a^{-3/5}$, where a_{\min} and a_{\max} define the boundary size of the grains (Mathis et al. 1977). Results from Weingartner & Draine (2001) indicate that in the interstellar medium the dust grains are composed of silicate species and

amorphous carbon. The size of such dust grains varies from $a_{\min} = 0.005$ to $a_{\max} = 0.25 \mu\text{m}$. In addition, inside dense clouds or in the star-forming regions the grains can be mixed due to physical processes such as turbulence. This assumption is adopted in this paper, as well as in previous papers in the literature (Ossenkopf & Henning 1994; Weingartner & Draine 2001; Pontoppidan et al. 2005). Additionally, there is observational evidence of the presence of large grains ($a \sim 1 \mu\text{m}$) inside dense clouds in the interstellar medium (Steinacker et al. 2011). In the current work, the presence of silicate grains with different sizes around Elias 29 were investigated: (i) $a_{\text{grain}} = 0.005\text{--}0.25 \mu\text{m}$, (ii) $a_{\text{grain}} = 0.025\text{--}0.70 \mu\text{m}$ from Beckford et al. (2008), and (iii) $a_{\text{grain}} = 0.25\text{--}1.0 \mu\text{m}$. The size range of the employed ice grains in this work was $a_{\text{ice}} = 0.0125\text{--}0.125 \mu\text{m}$. Figure 5 presents the opacities calculated for the grains used in this paper, considering case (ii) for dust grains.

2.3. Modeling Elias 29

A lot of parameters are necessary to model a young star, which means that high degeneracy is involved in the calculations. Previous papers from Robitaille et al. (2007), Gramajo et al. (2010), and Whitney et al. (2013) show that it is important to define a range of values for each parameter involved in the modeling process, and after that, to try to find the best set. For Elias 29, the parameters were constrained using observational results published in previous papers from Boogert et al. (2002a), Huélamo et al. (2006), Lommen et al. (2008), Beckford et al. (2008), and Miotello et al. (2014), and can be seen in Table 1.

To model the observed spectrum of Elias 29 and its images in the IR, a three-dimensional Monte Carlo radiative transfer code, RADMC-3D (Dullemond 2012), was used with the opacities described in the previous section. In this code, we assume that density structure for Elias 29 is axisymmetric, although the photons are able to interact in the three dimensions. This approximation makes the problem essentially 2D with coordinates (r, θ) , and thus, much less computationally heavy. The Monte Carlo procedure used to calculate the temperature of the system is described in Bjorkman & Wood (2001), and its result is used to determine the position of the ices, where they can survive in the solid phase, and to create the SEDs and images of Elias 29 in specific wavelengths. During the simulation, the Monte Carlo calculation incorporated absorption and isotropic scattering, and used the size aperture of $100''$ to build the SEDs. This aperture is necessary to compute the flux of entire system (disk and envelope), as we will show in the next sections.

Figure 6 shows a schematic diagram of the Elias 29 environment, together with the ionizing radiation due to the protostar and CRs. This paper focuses on the effects of CRs on ices observed toward Elias 29. This figure also shows the inclination angle of observation and the chemical scenarios seen toward Elias 29.

2.3.1. Central Object

Because Elias 29 is a protostar heavily embedded, the high obscuration prevents optical spectroscopic measurements of effective temperature T_{eff} . Thus, to characterize this kind of protostar, Myers & Ladd (1993) proposed to use the bolometric temperature T_{bol} . The values estimated for Elias

⁵ <http://www.strw.leidenuniv.nl/lab/databases/isodb/isodb.html>

⁶ <http://www.astro.uni-jena.de/Laboratory/OCDB/data/silicate/amorph/olmg50.lnk>

⁷ <http://www.astro.uni-jena.de/Laboratory/OCDB/data/carbon/cel800.lnk>

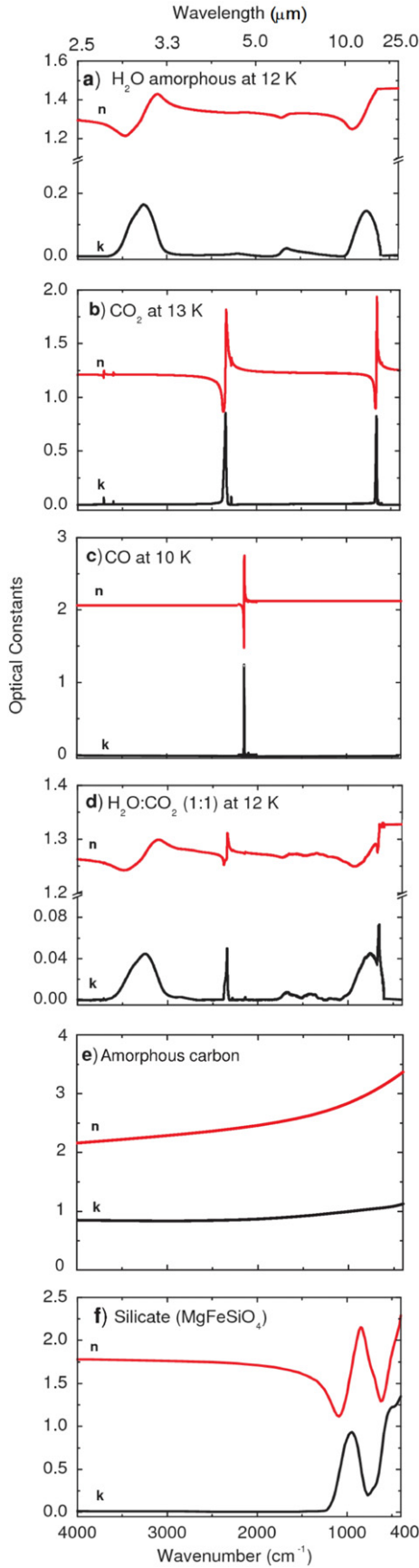


Figure 4. Optical constants n and k calculated using NKABS code, except for silicate and amorphous carbon.

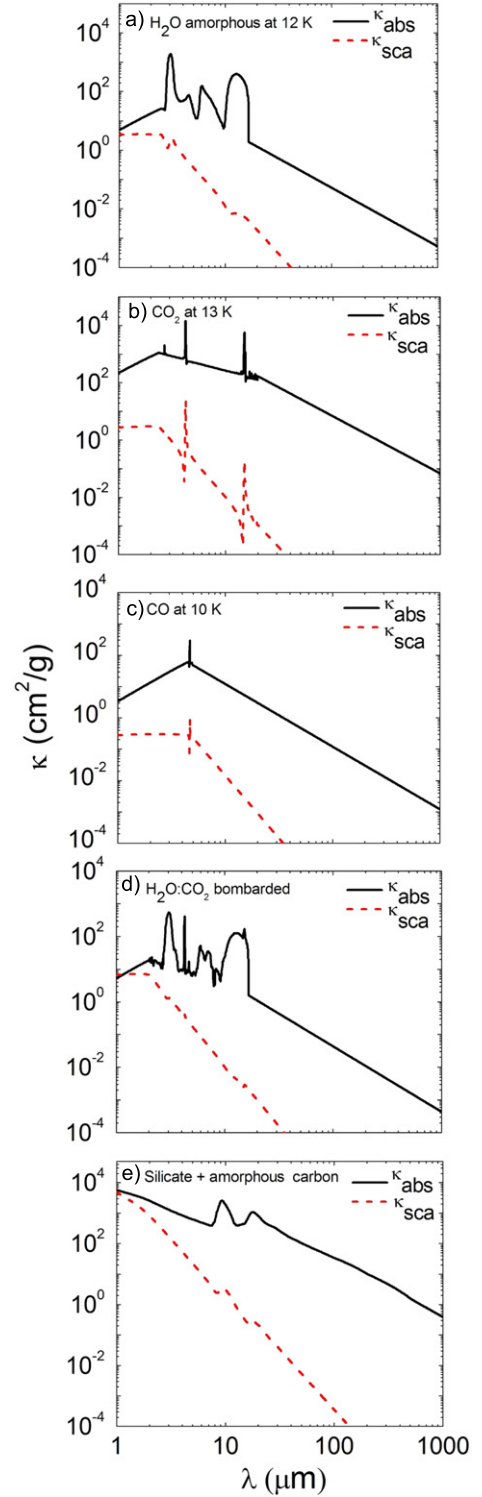


Figure 5. Opacities for ices and silicates with amorphous carbon. The continuous line represents the absorption opacity and the dashed line the scattering opacity.

29 in the literature are 410 K (Chen et al. 1995) and 390 K (Evans et al. 2003). In this paper an estimation of effective temperature was used for the Elias 29 protostar that was based on McClure et al. (2010), which employed the extinction law toward the ρ Ophiuchi cloud to determine the spectral type of several YSOs, and Miotello et al. (2014), which obtained data in longer wavelengths. From these observational constraints,

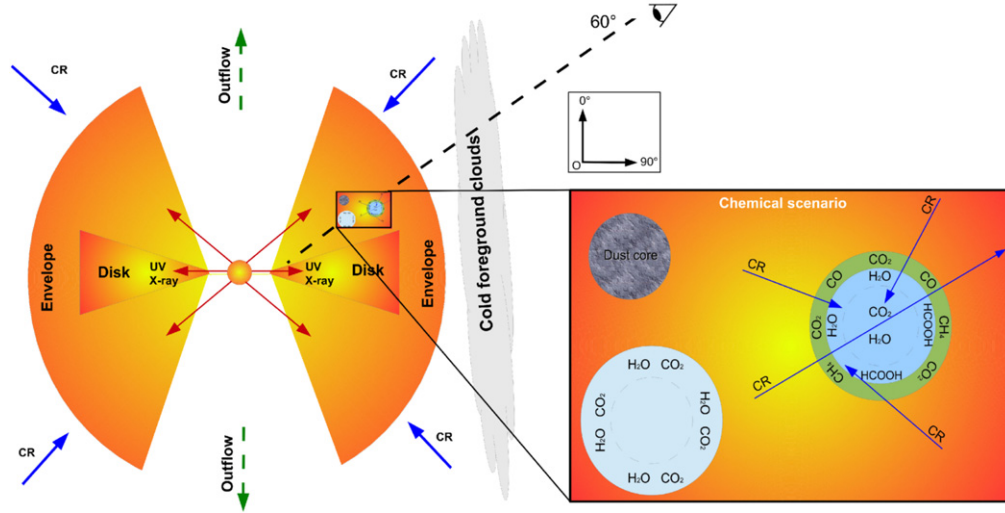


Figure 6. Schematic overview of the morphology and chemical scenario of Elias 29 employed in this paper. The line of sight crosses through the foreground clouds and envelope, indicating the angle $i = 60^\circ$, taking as reference the angles shown in the inset panel.

Table 1
Better Parameters Employed in Model 1 (Non-bombarded Ices) and Model 2 (Bombarded Ices)

Parameter	Description	Employed Value (see text)	Estimated Range	Literature Value
R (R_\odot)	Stellar radius	5.7	5–12	5.8 ^a , 5.9 ^b
T (K)	Stellar temperature	4880	4000–5000	4786 ^b , 4913 ^a
L (L_\odot)	Stellar luminosity	16.5	13–36	13.6 ^c , 16.3 ^b , 17.5 ^a 36 ^d
M_d (M_\odot)	Disk mass	0.003	0.002–0.007	<0.007 ^e
$R_{d,in}$ (AU)	Disk inner radius	0.36	fixed	0.25 ^f
$R_{d,out}$ (AU)	Disk outer radius	200	fixed	200 ^e
M_{env} (M_\odot)	Envelope mass	0.028	0.02–0.06	<0.058 ^e
$R_{env,in}$ (AU)	Envelope inner radius	0.36	fixed	...
$R_{env,out}$ (AU)	Envelope outer radius	6000	fixed	6000 ^g
θ_c ($^\circ$)	Cavity angle	30	25–55	40 ^h
d (pc)	Distance	120	100–160	125 ⁱ , 160 ^g

Notes.

- ^a McClure et al. (2010).
^b Miotello et al. (2014).
^c Evans et al. (2003).
^d Chen et al. (1995).
^e Lommen et al. (2008).
^f Simon et al. (1987).
^g Boogert et al. (2002a).
^h Beckford et al. (2008).
ⁱ de Geus et al. (1989).

the physical properties should be $T_{\text{eff}} = 4913$ K and $R = 5.8 R_\odot$, meaning that $L = 17.5 L_\odot$, and $T_{\text{eff}} = 4786$ K and $R = 5.9 R_\odot$, meaning that $L = 16.3 L_\odot$, respectively. In this paper, the considered ranges were $R = 5\text{--}12 R_\odot$ and $T = 4000\text{--}5000$ K. From our modeling, the better values were $T_{\text{eff}} = 4880$ K and $R = 5.7 R_\odot$, and $L = 16.5 L_\odot$.

2.3.2. Disk and Envelope Geometry

The images from Huélamo et al. (2006) constrain the flared disk up to around 175 AU. However, it is important to note that such a disk may have a non-flared (self shadowed) component at large radii that cannot be seen by the scattered light in the near-IR. Therefore, the images in the near-IR constrain a lower limit of the disk size if a non-flared part is present.

The Elias 29 disk was modeled by using a density structure defined by power law along the radius and a Gaussian function in height scale, given by

$$\rho_{\text{disk}}(r, \theta) = \frac{\Sigma_0 (r/R_0)^{-1}}{\sqrt{2\pi} H(r)} \exp \left\{ -\frac{1}{2} \left[\frac{r \cos \theta}{H(r)} \right]^2 \right\} \quad (1)$$

where θ is the angle from the axis of symmetry; Σ_0 is the surface density at outer radius R_0 , which is related with the disk mass, M_{disk} ; and $H(r)$ is the disk scale height, given by $H(r) = r \cdot H_0/R_0 \cdot (r/R_0)^{2/7}$, defined from the self-irradiated passive disk proposed by Chiang & Goldreich (1997).

The inner radius of the disk was calculated based on the sublimation temperature of the silicate, using $R_{\text{in}} = R_*(T_*/T_{\text{in}})^2$

from Dullemond & Monnier (2012). Assuming that the silicate grains sublimate at $T_{\text{in}} = 1500$ K, then $R_{\text{in}} = 0.36$ AU for Elias 29. Following Lommen et al. (2008) and Miotello et al. (2014), the outer radius of the disk $R_{\text{out}} = 200$ AU and the ratio $H_0/R_0 = 0.17$ were adopted in this paper.

Besides the disk, Elias 29 is surrounded by a large envelope, given the radial intensity profile obtained from the 1.3 mm map (Motte et al. 1998) modeled by Boogert et al. (2002a). This profile is better fit by the presence of the envelope extended up to 6000 AU in addition to the disk. To describe it we are considering a static envelope whose density is given by the following power law:

$$\rho_{\text{env}}(r) = \rho_0 \left(\frac{R_{\text{out}}}{r} \right)^{1.5} \quad (2)$$

where ρ_0 is the density at the outer radius.

Given the observations of the jets in Elias 29 (Gómez et al. 2003; Zhang et al. 2013), it is reasonable to consider a cavity in the envelope. The cavity aperture was constrained from near-IR images, combined with a linear polarimetry technique toward ρ Ophiuchi, taken from Beckford et al. (2008). For Elias 29, the opening angle of the cavity estimated in the K band is $\theta = 30^\circ$.

Table 1 summarizes the parameters used in Models 1 and 2, as well as the estimated range due to the degeneracy involved in the modeling.

2.3.3. Grain Spatial Distribution

More realistic scenarios for modeling protostellar disks and envelopes should consider the sublimation temperature of the silicates and ices, as well as the possibility of the radiation and temperature processing. Taking this into account, the silicate and ice grains should occupy specific regions around the protostar. The sublimation temperatures of the grains used in this paper can be found in the literature: (i) silicate—1500 K (Gail 2010), (ii) H_2O —150 K, CO_2 —75 K, CO —20 K (Collings et al. 2004), and (iii) $\text{H}_2\text{O}:\text{CO}_2$ bombarded, assumed to be 150 K.

Note, however, that frozen molecules trapped in H_2O ice will be desorbed at two different temperatures: (i) desorption of the species from the surface of the H_2O ice and (ii) desorption from molecules trapped inside the bulk of the H_2O ice (Collings et al. 2004). This means that volatile molecules can be placed at the inner regions of the protostellar disk (Visser et al. 2009) and, consequently, more subjected to radiative and thermal processing.

In this paper, the dust grains were used in the spatial grids and the ices were employed where the temperature was lower than the sublimation temperature. This procedure was performed by calculating the temperature of the structure by Monte Carlo methodology, first employing only the ice opacities. Next, this result was used to determine the position of each ice around Elias 29, and a new temperature was calculated to build the SED and images in the IR. This procedure showed that pure CO ice cannot be present in the envelope along the line of sight of Elias 29 due to low sublimation temperature, and would not be seen in the modeled spectrum. To reproduce the CO observed in Figure 1, we assume that all CO is trapped in H_2O ice. The assumption that all species are constrained to the disk and envelope is not very

realistic because a fraction of the ice should be placed in foreground clouds.

3. RESULTS

3.1. Spectral Energy Distribution

Figure 7 shows the SED for Model 1, employing only non-bombarded ices, similar to the one performed by Pontoppidan et al. (2005). Note however, that such modeling is able to reproduce many physical parameters of the protostar, but it was not able to reproduce the chemical changes induced by radiation (driven by CRs or high energy radiation) on the ice mantles, observed at wavelengths around $5.5\text{--}8.0\ \mu\text{m}$ and $15.15\text{--}15.25\ \mu\text{m}$. This means that, despite the strong bands observed in the Elias 29 SED (e.g., H_2O , CO_2 , CO , silicate) that were well fit by the modeling, weak features formed from ice chemistry cannot be probed by Model 1. On the other hand, the better model is shown in Figure 8, where the physical and chemical properties were reproduced. To reach this result, the presence of the bombarded ice ($\text{H}_2\text{O}:\text{CO}_2$) was fundamental to improve the chemistry of the modeling. Such processed ices were employed in this work in Model 2. In both models, the average abundances of the ices relative with H_2 and the dust mass of the disk and envelope were constrained from Boogert et al. (2000) and Lommen et al. (2008). Section 3.3 shows how the abundances were derived in this paper.

Figures 7(a) and 8(a) show the Elias 29 SED modeled with RADMC-3D covering $0.1\text{--}80,000\ \mu\text{m}$. This graphic also shows the (i) observational spectrum from *ISO* (black line), (ii) blackbody of the protostar without extinction (dotted black line), (iii) cold foreground clouds (blue and green dashed lines), and the (iv) photometric data from bands 2MASS (1.23, 1.66, 2.16 μm), *WISE* (3.35, 4.6, 11.56, 22.08 μm), *Spitzer* (8 μm), *IRAS* (12, 25, 60, 100 μm), and in the longer wavelengths (1.1 mm, 3 mm, 3 cm, 6 cm). The photometric data in the IR regime were taken from Infrared Science Archive⁸ and in the long wavelength regime from Lommen et al. (2008) and Miotello et al. (2014). Because the Elias 29 protostar is heavily embedded in its birthplace, we should consider the presence of the cold foreground (12–16 K) clouds (Boogert et al. 2002) to better simulate the observed spectrum after 80 μm . The foreground emission of cold clouds was added to the SED by hand, and is not part of the radiative transfer simulation. These clouds produce a modified blackbody emission at long wavelengths (Hildebrand 1983; Ward-Thompson et al. 2000), sometimes called graybody emission, and given by

$$S_\nu = \Delta\Omega B_\nu(T) [1 - e^{-\tau_\nu}] \quad (3)$$

where $\Delta\Omega$ is the solid angle of the source and $B_\nu(T)$ is the blackbody emission at temperature T . The optical depth is given by $\tau_\nu = k_\nu N_d$, where k_ν is the absorption mass coefficient given by $k_\nu = k_0(\nu/\nu_0)^\beta$ —where β is the opacity index—and N_d the mass column density of the dust toward the line of sight. Adopting the k_0 at 1.3 mm as $k_{1.3} = 0.01$ (taken from Figure 5, assuming a dust-to-gas ratio of 0.01), we performed the fit by using two graybodies to reproduce the Elias 29 SED at long wavelengths. Table 2 shows the better parameters obtained with the fit.

⁸ <http://irsa.ipac.caltech.edu>

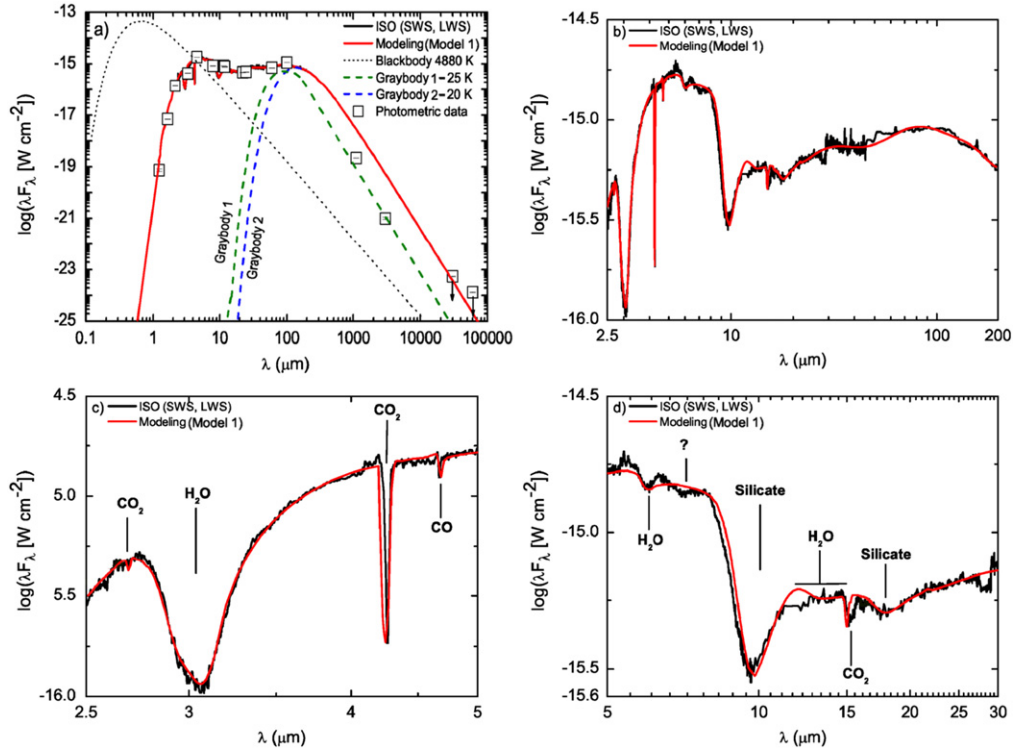


Figure 7. Modeling employing only unprocessed ices (Model 1) for the Elias 29 SED. The four panels show the spectral energy distribution of Elias 29 (black line), modeled by RADMC-3D (red line). (a) the dotted black line represents the blackbody associated with 4880 K, blue and green dashed lines are the graybody associated with the cold foreground clouds (20 and 25 K, respectively), and photometric measurements from near-IR to sub-millimeter taken from public archives. (b) Detail of panel (a), covering 2.5–200 μ m. (c) Detail of panel (b), covering 2.5–5.0 μ m. This panel also shows the absorption features of CO, CO₂, and H₂O. (d) Detail of panel (b), covering 5.0–30.0 μ m. This panel shows the presence of absorption bands of CO₂, H₂O, and silicate.

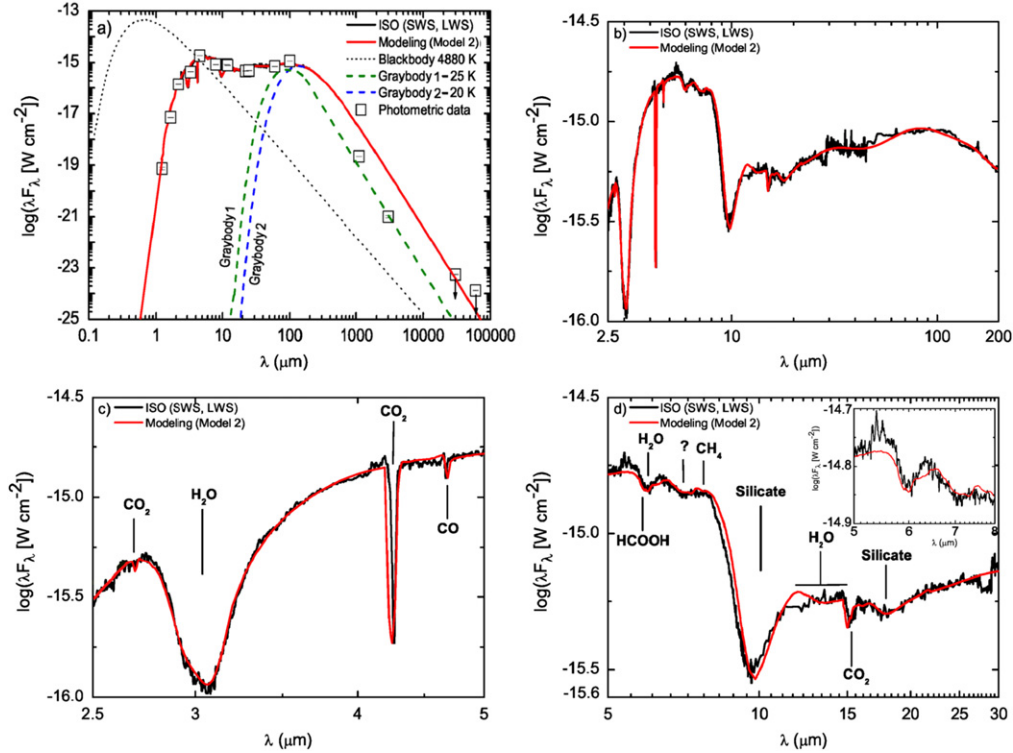


Figure 8. Better modeling employing processed ices (Model 2) for the Elias 29 SED. The lines and symbols are the same as Figure 7. However, in panel (d) the absorption range from 5.5 to 8.0 μ m was better fitted by Model 2, as is indicated by the presence of HCOOH and CH₄. The inset panel is a zoom in on the region of the fit.

Table 2
Parameters Obtained from Graybody Fitting Relative to Cold Foreground Clouds

Graybody	N_H (cm ⁻²) ^a	A_V (mag) ^b	$\Delta\Omega$ (sr)	β	T (K)
1	$(8.0 \pm 0.2) \times 10^{21}$	4.0 ± 1.0	$(1.7 \pm 0.1) \times 10^{-8}$	2	25.2 ± 1.3
2	$(1.2 \pm 0.3) \times 10^{22}$	6.0 ± 1.5	$(7.0 \pm 0.1) \times 10^{-7}$	2	20.2 ± 0.8

Notes.

^a Assuming a dust-to-gas ratio of 0.01.

^b Using the relation $N_H = 2 \times 10^{21} A_V \text{ cm}^{-2} \text{ mag}^{-1}$ from Bohlin et al. (1978).

Figures 7(a) and 8(a) also show that near-IR fluxes are over strong extinction by dust. From the difference between the blackbody of the protostar without extinction (dotted line) and the modeled blackbody (red line), the extinction calculated for the J band at $1.23 \mu\text{m}$ is $A_J = 15.3 \text{ mag}$. Assuming that visual extinction A_V is related with A_J by using $A_J = 0.282 A_V$ from Cambr  s et al. (2002), then the visual extinction toward Elias 29 is $A_V = 54.3 \text{ mag}$. Given the relation between the visual extinction and column density of hydrogen from Bohlin et al. (1978), $N_H = 1.3 \times 10^{23} \text{ cm}^{-2}$ toward line of sight of Elias 29. This value agrees with the estimate presented in Boogert et al. (2000), calculated as $N_H = 0.5\text{--}1.2 \times 10^{23} \text{ cm}^{-2}$. From McClure et al. (2010), it is possible calculate that $N_H = 0.8 \times 10^{23} \text{ cm}^{-2}$ for Elias 29.

Figures 7(b) and 8(b) show, in detail, the fitting (red line) covering $2.3\text{--}200 \mu\text{m}$ over the observational data from the *ISO* (black line). These panels highlight the good fit of the continuum from the near-IR to far-IR. Figures 7(c) and 8(c) present strong absorption bands of H_2O ($3.07 \mu\text{m}$), CO_2 (2.69 and $4.26 \mu\text{m}$), and CO ($4.67 \mu\text{m}$) ices. As discussed by Rocha & Pilling (2014) the observed absorption profile of H_2O clearly indicates its amorphous structure. Laboratory studies from Fraser et al. (2001) show that H_2O ice changes from the amorphous to crystalline phase at a temperature around 120 K. This means that the temperature where H_2O ice is condensed must be lower than 120 K. Figures 7(c) and 8(c) also show a small shift of the modeled band of CO_2 and CO compared with the observation. This happens because we are assuming that ice grains in the modeling have a spherical geometry, as proposed by the Mie theory. Studies from Boogert et al. (2002) show that if ellipsoidal grains, instead spherical ones, are assumed, such bands can be better fit.

Figures 7(d) and 8(d) show that the silicate is the most strong band in this range (9.8 and $18 \mu\text{m}$). Furthermore, ice grains containing molecules such as H_2O , CO_2 , HCOOH , and CH_4 observed toward Elias 29 (Boogert et al. 2000) also present vibrational modes in this part of the infrared spectrum. However, Figures 7(d) and 8(d) show that if only unprocessed ices are employed in the modeling (Model 1), the absorption bands between 5.5 and $8.0 \mu\text{m}$ are poorly fit. Otherwise, if a fraction of bombarded ice ($\text{H}_2\text{O}:\text{CO}_2$) is added to an unprocessed one (Model 2), the same range in the observed infrared spectrum of Elias 29 is better simulated. The inset graphic in Figure 8(d) shows a detailed zoom of the fitting between 5.5 and $8.0 \mu\text{m}$. Model 2 is also able to better fit the CO_2 absorption band at 15.15 and $15.25 \mu\text{m}$, compared with Model 1.

Figure 9(a) presents, with detail, the infrared spectrum of Elias 29, as well as the two Models developed by this work in the spectral region between 5.5 and $8.0 \mu\text{m}$. Several molecules have vibrational modes in this spectral region and, therefore, the laboratory experiments are very helpful to identify the

presence of specific molecules. First, the observed presence of a HCOOH ice, due to vibrational modes at $5.85 \mu\text{m}$ ($\text{C}=\text{H}$ stretch vibrational mode) and $7.25 \mu\text{m}$ due to CH deformation. Next, a deformation mode of CH_4 ice is also observed at $7.69 \mu\text{m}$. Additionally, some complex molecules may be associated with the absorption bands at 6.85 and $7.01 \mu\text{m}$. The band at $7.01 \mu\text{m}$ can be associated with the acetaldehyde molecule (CH_3CHO) due to the CH_3 deformation mode. Studies from Bennett et al. (2005) show that this molecule can be formed inside dense molecular clouds when the astrophysical ice interacts with CRs. On the other hand, the nature of the band at $6.85 \mu\text{m}$ is unclear. Usually in the literature this band has been associated with the NH_4^+ ion from Shutte & Khanna (2003). However, in this paper we have shown that this feature can arise from a mixture containing only $\text{H}_2\text{O}:\text{CO}_2$ bombarded by CR analogs. In the current methodology, the molecular composition of the employed mixture does not contain nitrogen atoms, and therefore, the feature at $6.85 \mu\text{m}$ is reproduced without the need for the NH_4^+ (ammonium) ion.

Additional evidence of the thermal processing of the ice inventory around Elias 29 can be observed from Figure 9(b). The CO_2 ice, pure and partially crystalline at low temperature ($\sim 10 \text{ K}$), is split into two narrow bands at 15.15 and $15.25 \mu\text{m}$. On the other hand, if the CO_2 ice is trapped in an H_2O ice forming a mixture ($\text{H}_2\text{O}:\text{CO}_2$) at low temperature, this absorption band presents a unique peak. However, laboratory experiments from Ehrenfreund et al. (1997) have shown that if a mixture of $\text{H}_2\text{O}:\text{CO}_2$ is submitted to increasing temperature, the split profile of CO_2 at 15.15 and $15.25 \mu\text{m}$ arises again. Such behavior has been associated with the ice segregation between apolar (CO_2) and polar (H_2O) molecules in the ice, which begins around 40 K. The second peak increases together with the increasing temperature. Figure 9(b) shows that if it is assumed to be pure crystalline CO_2 ice (Model 1), the band in $15.15\text{--}15.25 \mu\text{m}$ is poorly fitted. A better fit is reached if a thermally processed ice is present around Elias 29 (Model 2).

Figure 10 shows that the regime between 5.5 and $8.0 \mu\text{m}$ can be associated with several and other species that do not contain nitrogen atoms, as for example, aliphatic ethers (e.g., $\text{R1-OCH}_2\text{-R2}$) and related species. The problem of the complex molecules associated with this band is that strong absorption features in other wavelengths are missing. Pilling et al. (2010b) show that if an ice mixture containing NH_3 is bombarded by CR analogs, the absorption band at $6.85 \mu\text{m}$ also arises. However, the OCN^- is formed from ice bombardment as well, like in the Shutte & Khanna (2003) experiment. Perhaps this means that the band at $6.85 \mu\text{m}$ is associated with NH_4^+ ion when OCN^- is also formed. Otherwise, such band should be associated with the vibrational modes of C-H bonds. We conclude that Model 2 produces a better fit than Model 1, and in Table 3 compare the observed and modeled SEDs (Figure 8) at the central wavelengths of the ice absorption bands.

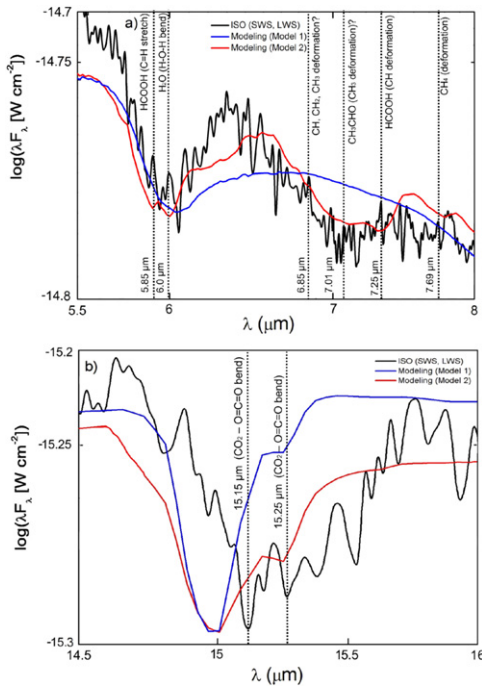


Figure 9. Evidence of the ice processing around Elias 29. Panel (a) shows the presence of HCOOH and CH₄. Furthermore, the range from 5.5 to 8.0 μm may be associated with C–H bonds, including CH₃CHO at 7.01 μm. Panel (b) shows evidence of the ice segregation in polar and apolar species.

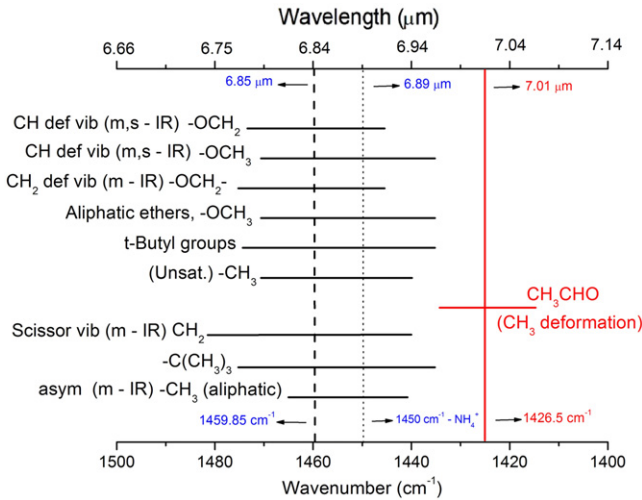


Figure 10. Diagram showing molecular species and some radicals containing H, C, and O that can be associated with the peak in the IR spectrum within the range of 5.5–8.0 μm. The black dashed line indicates the wavelength at 6.85 μm and the dotted black line indicates the central wavelength associated with the NH₄⁺ ion from Shutte & Khanna (2003). The red line indicates the CH₃ deformation associated with acetaldehyde (CH₃CHO).

3.2. Alternative Models for Grain Size Distribution

In this section, we show how the modeled SED of Elias 29 changes by adopting three regimes of dust grain sizes (silicate and amorphous carbon) and following the MRN size distribution (see Section 2.2.2 and Figure 5). It is important to observe that the size distribution of the ice remains the same and the adopted parameters are the same as Model 2. Figure 11(a) shows the Elias 29 SED between 2.5 and 30.0 μm, where the blue dashed line is the fitting employing the small grain distribution (0.005–0.25 μm) and the green dashed line is the

fitting employing large dust grains (0.25–1.0 μm). The better fit from near- to far-infrared is given by size grains between 0.25 and 0.70 μm. The other sizes can fit the observational data besides 8 μm, but are not able to model the spectrum at near-IR. The infrared region between 2.5 and 4.0 μm for different size dust grains is shown in Figure 11(b), and highlights the fitting in the near-IR. The extinction caused by small or large dust grains cannot reproduce the observational SED in all wavelengths. On the other hand, dust grains with intermediary size (0.25–0.70 μm) are able to model with accuracy the spectrum of Elias 29. This result is interesting because dust grains with a size of 0.6 μm were proposed by Boogert et al. (2000) to fit the Elias 29 SED, and with a size of 0.7 μm were observed toward Elias 29 by Beckford et al. (2008).

Indeed, the intermediary size dust grains, following the MRN distribution, were able to model the Elias 29 SED in this paper. However, some caveats should be mentioned about this section. Miotello et al. (2014) show that dust grains with millimeter size can be present in the Elias 29 envelope because they are necessary to fit the data at 1.1 mm and 3 mm from the Submillimeter Array (SMA) and ATCA, respectively. However by assuming the MRN distribution in this paper, large grains are not able to reproduce the Elias 29 SED. Perhaps a way to address this question would be a detailed study about the power law of the grains size distribution focusing on Elias 29. An additional caveat about this section is that we are considering that ice opacities are not affected by changing the dust grain size. Moreover, we are supposing that the size of the ices follows a strictly MRN distribution given by small grains.

3.3. Grain Abundances

To determine the average abundances relative to H₂, we employed the optical depth analysis explained in Boogert et al. (2000) because it allows us to calculate the abundances of numerous ice species that are formed with the ice bombardment. Briefly, it is defined as the continuum curve over the observational SED, as simulated by the blackbody fits. Next, the equation $\tau(\lambda) = \ln(I_0(\lambda)/I(\lambda))$ is used to determine the optical depth $\tau(\lambda)$ in each wavelength, where the observed spectrum and the adopted continuum are given by $I(\lambda)$ and $I_0(\lambda)$, respectively. Thereafter, knowing the optical depth and the band strength of each absorption, the column density is calculated. The column density for hydrogen calculated in this paper was $N_H = 1.3 \times 10^{23} \text{ cm}^{-2}$ (see Section 3.1). Lastly, the abundance of ices is given by the ratio between the column density of ices and H₂. However, unlike Boogert et al. (2000), such a methodology was applied by using the better model (Model 2), as shown in Figure 8. This methodology allows us to calculate the column density of the ices originated from the processing by CRs, but without the noise present in the observed spectrum. Table 4 shows the values obtained from this paper for Elias 29.

Figure 12(a) shows the average abundance of ices calculated from Model 2, compared with values from Boogert et al. (2000) and Lommen et al. (2008). Because we are assuming the presence of bombarded H₂O:CO₂ ice, the abundances of the processed material were also calculated. The necessary amount of processed H₂O and CO₂ ice to fit the observable spectrum was roughly 14 and 7%, respectively, relative to the total abundance employed in the modeling. The limits greater than observed by Boogert et al. (2000) are due to the bandwidth obtained from Model 2. CH₃OH and CH₃CHO are not shown in this figure because the presence of such molecules is

Table 3
Model 2 Comparison Between the Observed and Modeled λF_λ for Each Absorption Band of Ice and Silicate

λ (μm)	k (cm^{-1})	Assignment	λF_λ (Observed) (W cm^{-2}) ^a	λF_λ (Modeled) (W cm^{-2}) ^b	Error (%)
2.69	3708	CO ₂	$(5.92 \pm 0.05) \times 10^{-16}$	5.91×10^{-16}	0.17
3.07	3250	H ₂ O	$(1.38 \pm 0.03) \times 10^{-16}$	1.37×10^{-16}	0.72
4.26	2342	CO ₂	$(1.36 \pm 0.03) \times 10^{-16}$	1.38×10^{-16}	1.45
4.67	2139	CO	$(1.22 \pm 0.02) \times 10^{-15}$	1.21×10^{-15}	0.81
5.83	1715	HCOOH	$(1.47 \pm 0.03) \times 10^{-15}$	1.44×10^{-15}	2.01
6.00	1650	H ₂ O	$(1.45 \pm 0.01) \times 10^{-15}$	1.44×10^{-15}	0.70
6.85	1459	CH ₃ def?	$(1.48 \pm 0.08) \times 10^{-15}$	1.47×10^{-15}	0.67
7.01	1426	CH ₃ CHO?	$(1.40 \pm 0.01) \times 10^{-15}$	1.42×10^{-15}	1.41
7.67	1304	CH ₄	$(1.38 \pm 0.02) \times 10^{-15}$	1.41×10^{-15}	2.27
9.70	1031	Silicate	$(2.94 \pm 0.01) \times 10^{-15}$	3.00×10^{-15}	2.00
12.5	800	H ₂ O	$(5.55 \pm 0.41) \times 10^{-16}$	5.70×10^{-16}	2.63
15.15	660	CO ₂	$(4.53 \pm 0.29) \times 10^{-16}$	4.52×10^{-16}	0.22
15.25	655	CO ₂	$(4.78 \pm 0.28) \times 10^{-16}$	4.87×10^{-16}	1.84
18.00	555	Silicate	$(5.27 \pm 0.17) \times 10^{-16}$	5.20×10^{-16}	1.30

Note. The central wavelength and wavenumber, as well as the associated molecules, are presented in columns 1, 2, and 3, respectively. The λF_λ values are presented in columns 4 and 5, and the percentage error in column 6.

^a ISO (SWS, LWS) de Graauw et al. (1996) and Clegg et al. (1996).

^b This paper.

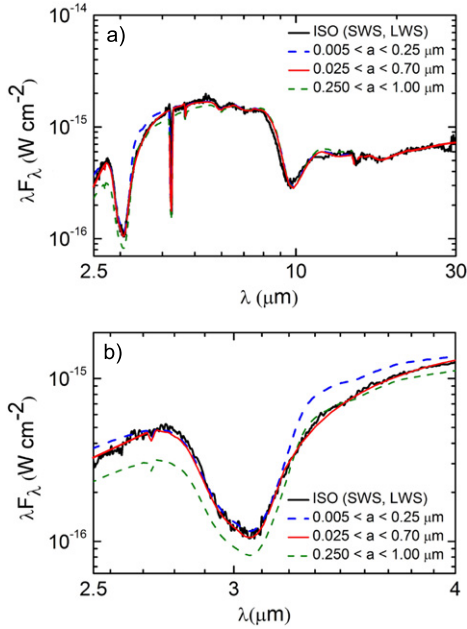


Figure 11. Modeling by using different size grains. Panel (a) presents the spectrum between 2.5 and 30 μm , showing that small and large grains cannot fit the observation. Panel (b) shows detail of panel (a) between 2.5 and 4.0 μm . The small grains (0.005–0.25 μm) can fit small wavelengths, but cannot fit longer wavelengths. On the other hand, large grains (0.25–1.0 μm) cannot fit the spectrum at near-IR and mid-IR. The better fit is given by intermediary size grains (0.025–0.7 μm).

uncertain in this paper. Figure 12(b) shows the mass of the disk and envelope used in Model 2, compared with values from Lommen et al. (2008). The upper limit proposed for Elias 29 is $M_{\text{disk}} \leq 0.007 M_\odot$ and $M_{\text{envelope}} \leq 0.058 M_\odot$. The values calculated from Model 2 were $M_{\text{disk}} = 0.003 M_\odot$ and $M_{\text{envelope}} = 0.028 M_\odot$ and are shown in Figure 12(b).

3.4. Density and Temperature Structure

Figures 13(a) and (b) present the density and temperature distribution for Model 2, emphasizing the disk and envelope,

respectively. Such parameters were necessary to determine the regions where the ices employed in Model 2 survive in the solid phase. The continuous lines in Figures 13(a) and (b) indicate the density contours for H₂ in cm^{-3} . Figure 13(a) shows that the disk density at the mid-plane reaches values of more than 10^7 cm^{-3} , while in Figure 13(b), the density of the envelope close to the edge is equivalent to 140 cm^{-3} . The dashed lines represent the snow lines, which are the limits that define regions around the protostar where pure molecules survive in the solid phase. The inset panels in Figure 13(a) show detail of CO₂ and H₂O snow lines.

The temperature map calculated from Model 2, using the RADMC-3D code, allows to conclude that water-rich ices are present in the Elias 29 disk, just beside 8 AU, and in the envelope beyond 14 AU. This difference is due to density distribution on the disk and envelope. On the other hand, the more volatile, pure CO₂ ice stay in the disk and envelope beyond 20 and 80 AU, respectively. However, pure CO ice just survives in the solid phase far away from the radiation source. Due to Elias 29's disk inclination of $i = 60^\circ$, Figure 13(b) allows us to conclude that most pure CO ice observed toward Elias 29 should not be placed in their envelope due to high temperature, but in cold foreground clouds. This confirms the observation of CO in the gas phase toward Elias 29, as shown in Boogert et al. (2000). Although it has been considered that all CO ice is trapped in the H₂O ice, the most realistic scenario should take into account the radiative transfer in the foreground clouds containing pure CO ice.

There is evidence in the literature that snow lines move away along the evolution of protostars from class I to photosphere objects. Zhang et al. (2013) report different water abundances in the TW HYA protoplanetary disk. The authors observed that between 0.5 and 4 AU, the abundance was calculated in 10^{-6} per H₂, while after 4 AU it was calculated in 10^{-4} per H₂. This observational data mean that with time in passive disks, like Elias 29, the inner disk becomes very dry, while a significant ice reservoir is formed at large radii of the disks formed.

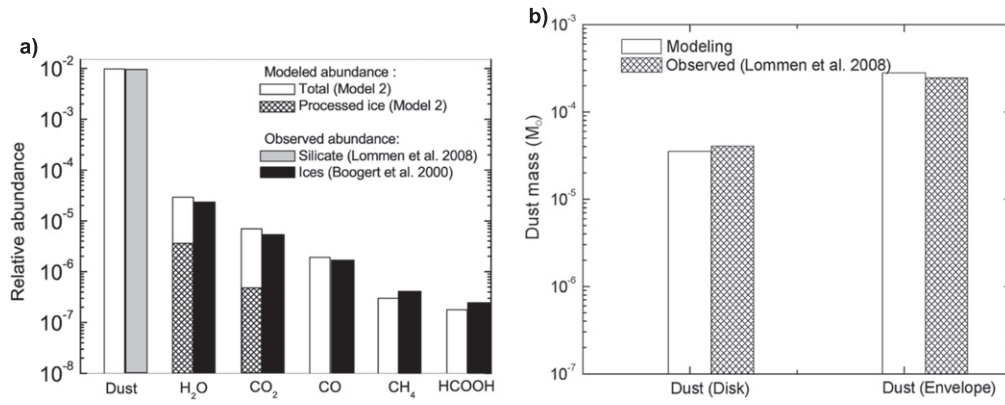


Figure 12. (a) Relative abundance of each molecular specie used in the modeling compared with observational data from other authors. The white bars represent the total abundance relative to H_2 that is necessary to fit the Elias 29 spectrum, assuming a dust-to-gas ratio equal to 0.01. Likewise, the gray bar is the dust-to-gas ratio taken from Lommen et al. (2008). The hatched bars represent the abundance of the ice processed by ionizing radiation, used in Model 2. The black bars show the abundances of the ices found in Boogert et al. (2000) for Elias 29 obtained from the ratio between the column density of the ices and the column density of H_2 . (b) Dust mass (in solar mass) employed in Model 2 (white bars) for the disk and envelope compared with observational data from Lommen et al. (2008; hatched bars).

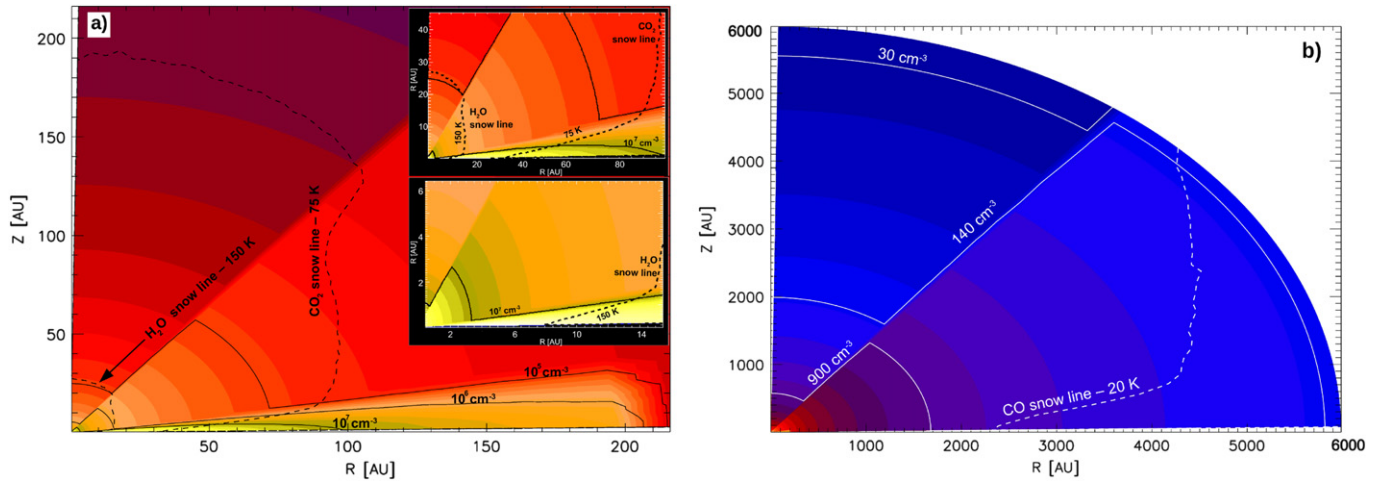


Figure 13. Structure of the H_2 density (continuous line) in cm^{-3} and selected temperature in K (dashed line) for the Elias 29 protostar. The color code indicates changes in the H_2 density. (a) Region limited to 210 AU to emphasize the disk. The two dashed lines indicate temperatures of 150 and 75 K, respectively. Inset panels show with detail the inner part of the protoplanetary disk. (b) Region limited to 6000 AU to emphasize the envelope. The density of that region is very low in relation to the disk, and the dashed line indicates the temperature of 20 K.

Table 4
Average Abundances of Ices Observed Toward Elias 29 Calculated from Model 2, Compared with Values Obtained in the Literature

Ice Species	Column Density ($10^{18} cm^{-2}$)	Abundance Relative to H_2 gas	Abundance Relative to H_2 gas (Literature) ^a	Wavelength— μm (Wavenumber— cm^{-1})	Band Strength ($cm molecule^{-1}$)
H_2O	3.50	2.9×10^{-5}	2.5×10^{-5}	3.07 (3250)	2.0×10^{-16b}
CO_2	0.84	7.0×10^{-6}	5.6×10^{-6}	4.26 (2342)	7.6×10^{-17b}
CO	0.21	1.9×10^{-6}	1.7×10^{-6}	4.67 (2139)	1.1×10^{-17b}
HCOOH	0.02	1.8×10^{-7}	$<2.5 \times 10^{-7}$	5.83 (1715)	6.7×10^{-17c}
CH_4	0.04	3.1×10^{-7}	$<4.1 \times 10^{-7}$	7.67 (1304)	7.3×10^{-18d}
CH_3OH	0.06	1.3×10^{-7}	$<6.3 \times 10^{-7}$	6.85 (1460)	1.2×10^{-17e}
CH_3CHO	0.004	3.2×10^{-8}	...	7.01 (1426)	3.6×10^{-18f}

^a Boogert et al. (2000).

^b Gerakines et al. (1995).

^c Schutte et al. (1999).

^d Kerkhof et al. (1999).

^e Assumed to be the CH_3 deformation of CH_3OH at 6.85 μm .

^f Bennett et al. (2005)—Assumed to be the CH_3CHO molecule.

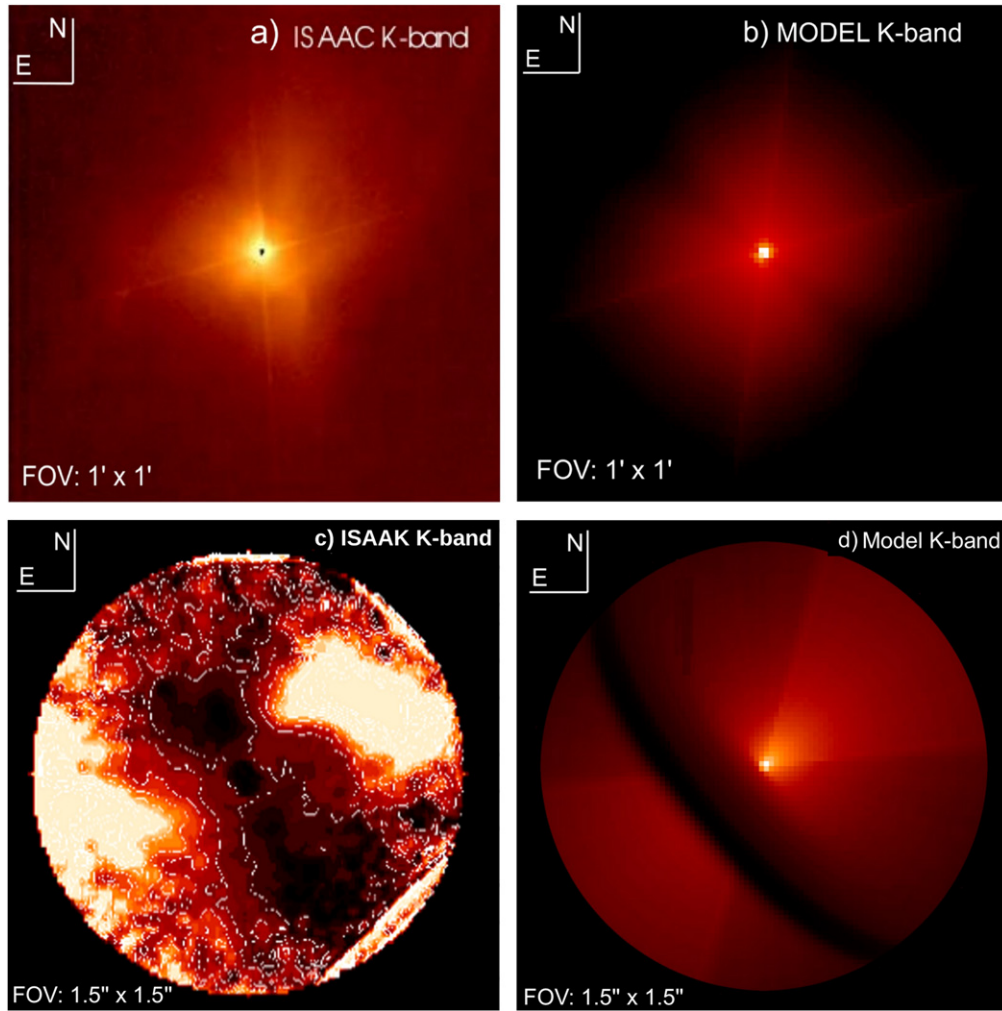


Figure 14. Comparison between the observed and modeled images of Elias 29 in the infrared with the same field of view (FOV). (a) Elias 29 structure in a field of view equal to $1' \times 1'$ on the K band from ISAAC (Infrared Spectrometer And Array Camera), modified from Huélamo et al. (2005). (b) Modeled image on the K band, assuming the parameters of Model 2. (c) Normalized K -band polarization image emphasizing the disk of Elias 29. (d) Modeled image calculated from Model 2, without polarization.

3.5. Infrared Images

In this section we present the images in the IR, modeled with RADMC-3D, assuming a more realistic scenario (Model 2). The images were created by using the 1×10^9 photon package to run the Monte Carlo simulation. Then, the average intensity over width $\Delta\lambda$ of each filter was calculated.

The comparison between the observed images of Elias 29 in the infrared and modeled images (Model 2) are shown in Figure 14. Figure 14(a) presents the observed image in the K band taken from Huélamo et al. (2006) with $\text{FOV} = 1' \times 1'$. Figure 14(b) shows the simulated image in the same band and in the same FOV employing Model 2. The difference in the brightening between the observed and modeled images may be explained by an external illumination originating from nearby stars. Whitney et al. (2013) show that the external illumination can dominate if the central source luminosity is very low, and/or the outer radius of the envelope is very large. From Figure 13(b), we can observe that the large model envelope around Elias 29 is very cold near the edge and therefore exhibits low surface brightness in the near-infrared. On the other hand, the presence of external illumination around Elias 29 would increase the temperature of the envelope, and

consequently, increase the near-IR surface brightness. Furthermore, Figures 14(c) and (d) emphasize the disk structure of Elias 29 in a $\text{FOV} = 1.5'' \times 1.5''$. The observed image was taken from Huélamo et al. (2006) by using the polarimetric technique with the NACO instrument. This image represents the normalized K -band polarization. The dark lane is seen in the NE–SW direction, in addition to scattering the radiation in the NW–SE. The modeled image presents the extinction of the radiation due to disk, as well as the scattering. From this image, we can conclude which dark structure seen from observations is due to the surface of the disk.

Figures 15 and 16 show the resolved images, emphasizing the disk structure and the envelope in the IR, respectively, as well as the intensity in logarithmic scale. All panels in Figure 15 have an FOV of $3/3 \times 3/3$ or $400 \text{ AU} \times 400 \text{ AU}$, while Figure 16 illustrates an FOV of $100'' \times 100''$ or $12,000 \text{ AU} \times 12,000 \text{ AU}$, assuming a distance of 120 pc, obtained from SED modeling.

4. CONCLUSIONS

We present a realistic theoretical model of the spectrum and image of the Elias 29 protostar using an axisymmetric, Monte

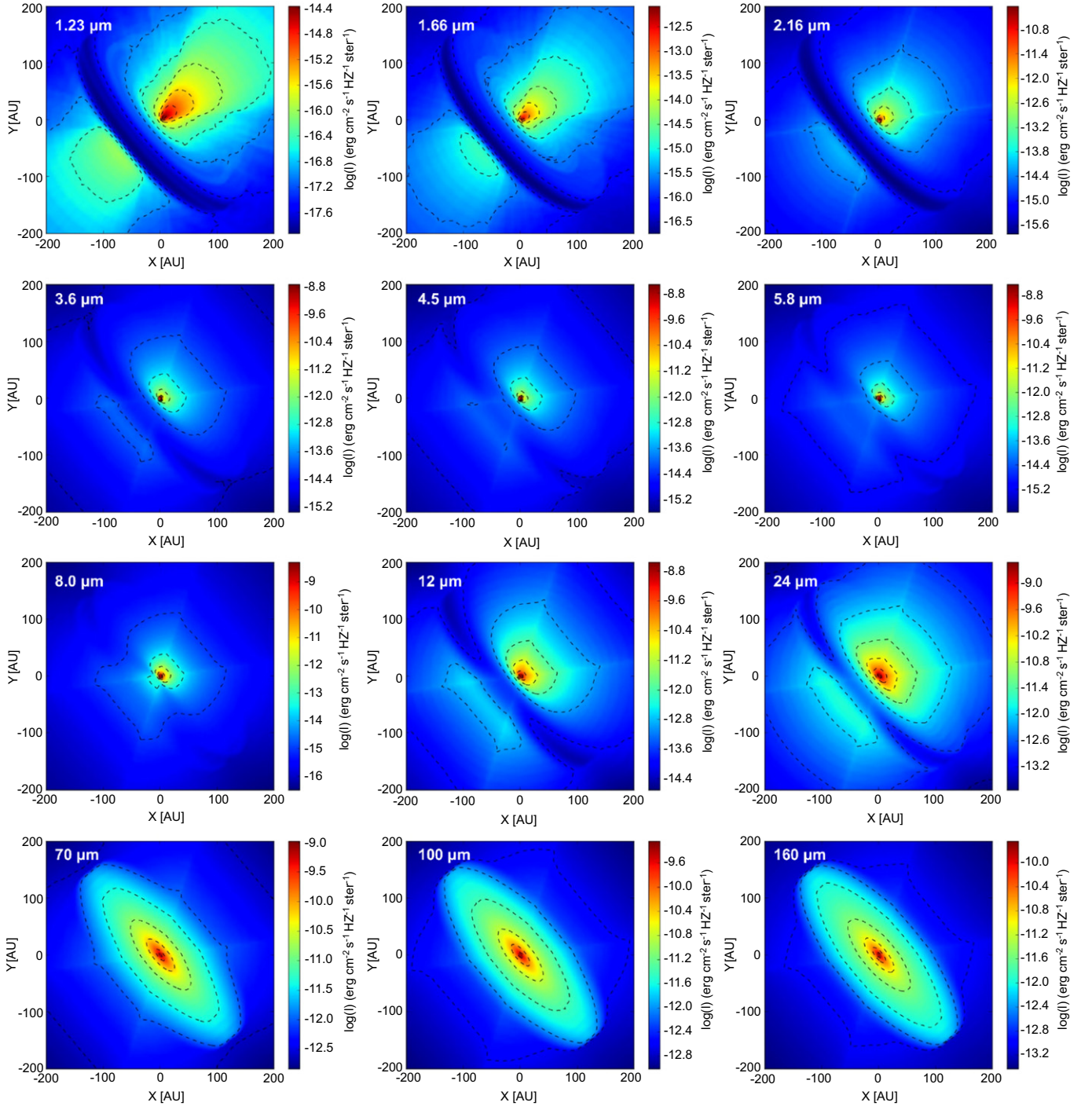


Figure 15. Resolved images for Elias 29, modeled using the RADMC-3D code. The layers present the intensities in $\text{ergs cm}^{-2} \text{s}^{-1} \text{Hz}^{-1} \text{sr}^{-1}$ for images ranging from near- to far-IR, and the contours correspond to values on the color bar. Each layer has a field of view of $3\frac{1}{3} \times 3\frac{1}{3}$ or $400 \text{ AU} \times 400 \text{ AU}$. The inclination of the protoplanetary disk relative to the line of sight is easily observed at low wavelengths (the the upper panels in this figure). An illustration of the modeled scenario is given in Figure 6.

Carlo radiative transfer code. An important characteristic of this paper was the use of radiative and thermal processed ices by high energy CRs, unlike previous works. The main conclusions obtained in this paper are summarized as follows.

1. The better model obtained for this YSO indicates that Elias 29 is better explained by a class I protostar in the late accretion phase. Furthermore, Elias 29 should be surrounded by a disk, with inclination close to 60° , to

reproduce the observed SED and image in near-IR. Moreover, the environment of Elias 29 is better reproduced by considering grains larger than observed in the interstellar medium, but somewhat lower than observed in dense regions of molecular clouds. Furthermore, a large fraction of the H_2O -rich ices observed toward Elias 29 are likely found in the cooler envelope regions outside the H_2O snow line. On the other hand, the

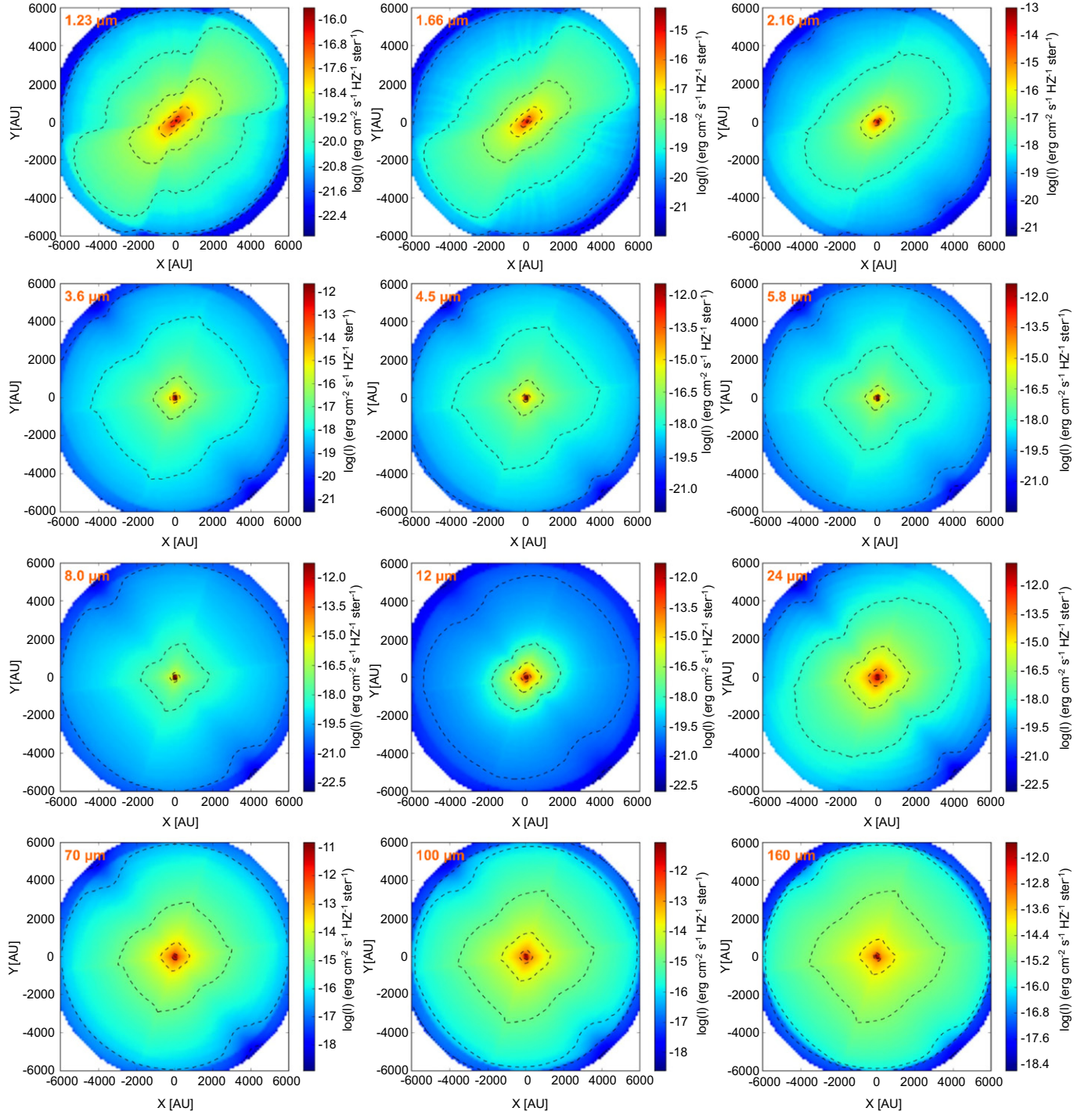


Figure 16. Resolved images for Elias 29, modeled using the RADMC-3D code. The layers present the intensities in $\text{ergs cm}^{-2} \text{s}^{-1} \text{Hz}^{-1} \text{sr}^{-1}$ for images ranging from near- to far-IR and the contours correspond to values on the color bar. Each layer has a field of view of $100'' \times 100''$ or $12,000 \text{ AU} \times 12,000 \text{ AU}$.

envelope is mostly too warm to support CO ice, implying most of the CO ice must be placed in foreground clouds.

2. There strong evidence that the ices around Elias 29 have been processed by high energy CRs and by temperature, which differs from the interpretation in Boogert et al. (2002a). The fingerprint of this processing can be found from the presence of HCOOH , CH_3CHO , and CH_4 , due to interaction of the H_2O and CO_2 ices with high energy cosmic rays. Moreover, the band at $6.85 \mu\text{m}$ observed in the Elias 29 spectrum can be associated with vibrational

modes of C–H bonds, instead of NH_4^+ , due to the absence of the absorption feature associated with OCN^- . Additionally, the ice segregation observed in 15.15 and $15.25 \mu\text{m}$ is more evidence that the thermal processing is induced by CRs.

3. The image modeled in the K band presents a good agreement with the observed image from the ISAAC telescope and with results from Huélamo et al. (2006) for $\text{FOV} = 1' \times 1'$ and $\text{FOV} = 1.5' \times 1.5'$. The resolved images of the disk also present a dark lane in the near-IR,

as observed in Huélamo et al. (2006). Additionally, the images emphasizing the envelope show characteristics of a bipolar cavity, as observed in Elias 29.

4. This paper shows the importance of combining the radiative transfer simulations with laboratory data of processed astrophysical ices to understand the absorption features of spectra of YSOs. Such a procedure highlights the importance of CRs to drive the formation of complex molecules around protostars.

We thank the anonymous referee for a careful review of the paper that allowed for its improvement. The authors also acknowledge the financial support from FAPESP (DR 2013/07657-5 and JP 2009/18304-0) and Ms. Alene Alder Rangel for the English revision of this manuscript.

REFERENCES

- Beckford, A. F., Lucas, P. W., Chrysostomou, A. C., et al. 2008, *MNRAS*, **384**, 907
- Bennett, C. J., Jamieson, C. S., Osamura, Y., et al. 2005, *ApJ*, **624**, 1097
- Bjorkman, J. E., & Wood, K. 2001, *ApJ*, **554**, 615
- Bohlin, R. C., Savage, B. D., & Drake, J. F. 1978, *ApJ*, **224**, 132
- Boogert, A. C. A., Blake, G. A., & Tielens, A. G. G. M. 2002, *ApJ*, **577**, 271
- Boogert, A. C. A., Hogerheijde, M. R., Ceccarelli, C., et al. 2002a, *ApJ*, **570**, 708
- Boogert, A. C. A., Pontoppidan, K. M., Knez, C., et al. 2008, *ApJ*, **678**, 985
- Boogert, A. C. A., Tielens, A. G. G. M., Ceccarelli, C., et al. 2000, *A&A*, **360**, 683
- Cambrésy, L., Beichman, C. A., Jarrett, T. H., et al. 2002, *AJ*, **123**, 2559
- Chen, H., Myers, P. C., Ladd, E. F., & Wood, D. O. S. 1995, *ApJ*, **445**, 377
- Chiang, E. I., & Goldreich, P. 1997, *ApJ*, **490**, 368
- Clegg, P. E., Ade, P. A. R., Armand, C., et al. 1996, *A&A*, **315**, L38
- Cleeves, L. I., Bergin, E. A., Alexander, C. M. O'D., et al. 2014, *Sci*, **345**, 1590
- Collings, M. P., Anderson, M. A., Chen, R., et al. 2004, *MNRAS*, **354**, 1133
- de Geus, E. J., de Zeeuw, P. T., & Lub, J. 1989, *A&A*, **417**, 159
- de Graauw, Th., Haser, L. N., Beintema, D. A., et al. 1996, *A&A*, **315**, L49
- Demyk, K., Dartois, E., D'Hendecourt, L., et al. 1998, *A&A*, **339**, 553
- Diolaiti, E., Bendinelli, O., Bonaccini, D., et al. 2000, *A&AS*, **147**, 335
- Dullemond, C. P., & Monnier, J. D. 2012, *ARA&A*, **48**, 205
- Ehrenfreund, P., Boogert, A. C. A., Gerakines, P. A., et al. 1997, *A&AS*, **328**, 649
- Elias, J. H. 1978, *ApJ*, **224**, 857
- Enoch, M. L., Evans, N. J., II, Sargent, A. I., et al. 2009, *ApJ*, **692**, 973
- Evans, N. J., Allen, L. E., Blake, G. A., et al. 2003, *PASP*, **115**, 965
- Fazio, G. G., Hora, J. L., Allen, L. E., et al. 2003, *ApJS*, **154**, 10
- Fraser, H. J., Collings, M. P., McCoustra, M. R. S., et al. 2001, *MNRAS*, **327**, 1165
- Gail, H. P. 2010, in *Astromineralogy*, ed. T. Henning, II, Vol. 815, (2nd ed.; Berlin: Springer), 61
- Gerakines, P. A., Shutte, W. A., Greenberg, J. M., et al. 1995, *A&A*, **296**, 810
- Gómez, M., Stark, D. P., Whitney, B. A., et al. 2003, *ApJ*, **126**, 863
- Gramajo, L. V., Whitney, B. A., Gómez, M., et al. 2010, *ApJ*, **139**, 2504
- Henning, T., & Semenov, D. 2013, *ChRv*, **113**, 9016
- Hildebrand, R. H. 1983, *QJRAS*, **24**, 267
- Hora, J. L., Carey, S., Surace, J., et al. 2008, *PASP*, **120**, 1233
- Huélamo, N., Brandner, W., Wolf, S., et al. 2006, in *The Planet-Disc Connection 2006* (Cambridge: Institute of Astronomy), 9
- Hudson, R. L., Moore, M. H., & Gerakines, P. A. 2001, *ApJ*, **550**, 1140
- Kenyon, S. J., Whitney, B., Gómez, M., & Hartmann, L. 1993, *ApJ*, **414**, 773
- Kerkhof, O., Shutte, W. A., & Ehrenfreund, P. 1999, *A&A*, **346**, 990
- Lada, C. J. 1987, in *IAU Symp. 115, Star Forming Regions*, ed. M. Peimbert, & J. Jugaku (Cambridge: Cambridge Univ. Press), 1
- Lada, C. J., & Wilking, B. A. 1984, *ApJ*, **287**, 610
- Lommen, D., Jørgensen, J. K., van Dishoeck, E. F., et al. 2008, *A&A*, **481**, 141
- Mathis, J. S., Rimpl, W., & Nordsieck, K. H. 1977, *ApJ*, **217**, 425
- McClure, M. K., Furlan, E., Manoj, P., et al. 2010, *ApJS*, **188**, 75
- Megeath, S. T., Allen, L. E., Gutermuth, R. A., et al. 2004, *ApJS*, **154**, 367
- Miotello, A., Testi, L., Lodato, G., et al. 2014, *A&A*, **567**, A32
- Motte, F., Andre, Ph., & Neri, R. 1998, *A&A*, **336**, 150
- Myers, P. C., & Ladd, E. E. 1993, *AJ*, **413**, L47
- Öberg, K. I., Boogert, A. C. A., Pontoppidan, K. M., et al. 2011, *ApJ*, **740**, 109
- Ossenkopf, V., & Henning, T. 1994, *A&A*, **291**, 943
- Pilling, S., Andrade, D. P. P., da Silveira, E. F., et al. 2012, *MNRAS*, **423**, 2209
- Pilling, S., Duarte, E. S., Domaracka, A., et al. 2011, *PCCP*, **13**, 15755
- Pilling, S., Seperuelo Duarte, E., da Silveira, E. F., et al. 2010, *A&A*, **509**, A87
- Pilling, S., Seperuelo Duarte, E., Domaracka, A., et al. 2010, *A&A*, **523**, A77
- Pontoppidan, K. M., Dullemond, C. P., van Dishoeck, E. F., et al. 2005, *ApJ*, **622**, 463
- Robitaille, T. P., Whitney, B. A., Indebetouw, R., et al. 2007, *ApJS*, **169**, 328
- Rocha, W. R. M., & Pilling, S. 2014, *SA&A*, **123**, 436
- Simon, M., Howell, R. R., Longmore, A. J., et al. 1987, *ApJ*, **320**, 344
- Schutte, W. A., Boogert, A. C. A., Tielens, A. G. G. M., et al. 1999, *A&A*, **343**, 966
- Schutte, W. A., & Khanna, R. K. 2003, *A&A*, **398**, 1049
- Steinacker, J., Pagani, L., Bacmann, A., et al. 2011, *A&A*, **511**, A9
- Tielens, A. G. G. M., & Charnley, S. B. 1997, *OLEB*, **27**, 23
- van Dishoeck, E. F., & Blake, G. A. 1998, *ARA&A*, **36**, 317
- Visser, R., van Dishoeck, E. F., Doty, S. D., et al. 2009, *A&A*, **495**, 881
- Ward-Thompson, D., Zylka, R., Mezger, P. G., et al. 2000, *A&A*, **355**, 1122
- Weingartner, J. C., & Draine, B. T. 2001, *ApJ*, **548**, 296
- Whitney, B. A., Kenyon, S. J., & Gómez, M. 1997, *ApJ*, **485**, 703
- Wilking, B. A., & Lada, C. J. 1983, *ApJ*, **271**, 698
- Whitney, B. A., Robitaille, T. P., Bjorkman, J. E., et al. 2013, *ApJS*, **207**, 30
- Whittet, D. C. B. 1974, *MNRAS*, **168**, 371
- Zhang, K., Pontoppidan, K. M., Salyk, C., & Blake, G. A. 2013, *ApJ*, **766**, 82
- Zhang, M., Brandner, W., Wang, H., et al. 2013, *A&A*, **553**, A41